Sustainable Energy & Fuels

ROYAL SOCIETY OF CHEMISTRY

PAPER

View Article Online
View Journal | View Issue

Check for updates

Cite this: *Sustainable Energy Fuels*, 2025, **9**, 2951

Transition metal-based coordination polymers of bipyridyl-ethylene for sunlight-driven photocatalytic CO_2 reduction into CO†

A. Abidi, *[abc] T. A. Quach,[d] M. Essalhi, [abe] D. Chartrand, [f] T. O. Do, [d] S. Barnabé*[abc] and M. Cibian *[ab]

Herein, three transition metal-based coordination polymers (**CoBpe**, **NiBpe**, and **CuBpe**) were synthesized *via* solvothermal reactions by combining the organic ligand 1,2-di(4-pyridyl) ethylene (**Bpe**) with cobalt(II), nickel(II), and copper(II) ions, respectively. Single crystal X-ray diffraction (SCXRD) characterization revealed the isostructurality of the cobalt- and nickel-based compounds, which crystallize in a monoclinic system and form a 1D ladder topology with interpenetrated square grids, while the copper derivative forms a linear chain topology within a triclinic crystal system. These structural differences are attributed to variations in synthesis conditions and counter anions. The materials presented herein exhibit optical and photoelectrochemical properties highlighting their semiconductor characteristics. They were used as catalysts for CO_2 reduction to CO, in photocatalytic systems with $[Ru(bpy)_3]Cl_2$ as photosensitizer (PS) and triethanolamine (TEOA) as sacrificial electron donor (SED), under simulated solar irradiation. **CoBpe** achieved a CO production rate of 287 μmol g^{-1} h^{-1} (4-hour experiment) and 410 μmol g^{-1} h^{-1} (8-hour experiment), placing itself as a competitive candidate among similar systems.

Received 8th February 2025
Accepted 23rd April 2025

DOI: 10.1039/d5se00195a

rsc.li/sustainable-energy

Open Access Article. Published on 30 2025. Downloaded on 29.11.2025 13:58:24.
This article is licensed under a Creative Commons Attribution-NonCommercial 3.0 Unported Licence.

Introduction

In recent years, the rapid growth in population and the excessive consumption of fossil fuels have led to a significant increase in anthropogenic CO_2 emission, triggering alarming consequences (*e.g.*, energy crisis, catastrophic weather patterns, ecosystem destruction).[1,2] In response, numerous measures have been implemented to tackle the problem and reduce the reliance on fossil fuels, such as shifting to renewable energy sources (*e.g.*, solar, wind, biomass) and introducing new policies to curb carbon footprints.[3] In addition, proactive technologies such as carbon capture and storage (CCS)[4] have been deployed to capture CO_2 from industrial fumes. However, this promising pathway remains challenging due to the high stability of CO_2 molecules (C=O bond energy: 750 kJ mol^{-1}).[5,6]

Furthermore, over the last decades, significant efforts have been devoted to converting CO_2 into feedstock fuels and value-added products (*e.g.*, formic acid,[7,8] methanol,[9,10] methane,[11] carbon monoxide) using photochemical processes. However, significant challenges remain, particularly in terms of efficiency, selectivity, and stability.[12–16] Mimicking natural photosynthesis, artificial sunlight-driven systems have evolved as an efficient way to remediate environmental issues.[17–19] The basis for developing artificial photosynthetic systems were set in 1972 by Fujishima and Honda, who utilized titanium dioxide (TiO_2) as a photocatalyst for water splitting under sunlight irradiation.[20] This innovation paved the way for numerous advanced photocatalytic applications, including dye degradation (methyl violet (MV),[21] rhodamine B (RhB)[22]), hazardous waste removal,[23] air and water purification,[24,25] and CO_2 photoreduction.[26] This light-driven process occurs when light strikes the photocatalyst's surface, usually semiconductor materials,[27] creating photogenerated charge carriers (electron–hole pairs), leading to a sequence of redox reactions. Moreover, due to their optical and redox properties, as well as thermal and solvent stability, various semiconductor materials have been used as photocatalysts for CO_2 reduction, such as metal oxides (*e.g.*, TiO_2, ZnO, SiO_2, WO_3),[28] metal sulfides (CdS, ZnS),[29] metal nitrides (GaN, TiN),[30] perovskites, ($BaTiO_3$, CaTiO),[31] Z-scheme heterojunctions,[32] Covalent-Organic Frameworks (COFs),[33] Metal–

[a]*Département de Biochimie, Chimie, Physique et Science Forensique, Université du Québec à Trois-Rivières, Trois-Rivières, Québec, G9A 5H7, Canada. E-mail: adela.abidi@uqtr.ca; simon.barnabé@uqtr.ca; mihaela.cibian@uqtr.ca*

[b]*Institut de Recherche sur l'hydrogène (IRH), Université du Québec à Trois-Rivières, Trois-Rivières, Québec, G9A 5H7, Canada*

[c]*Institut d'innovations en Écomatériaux, Écoproduits et Écoénergies à Base de Biomasse (I2E3), Université du Québec à Trois-Rivières, Trois-Rivières, Québec, G9A 5H7, Canada*

[d]*Département de Génie Chimique, Université de Laval, Québec, Québec G1V 0A6, Canada*

[e]*Interdisciplinary Research Center for Hydrogen Technologies and Carbon Management, King Fahd University of Petroleum & Minerals, Dhahran 31261, Saudi Arabia*

[f]*Département de Chimie, Université de Montréal, Montréal, Québec, H3C 3J7, Canada*

† Electronic supplementary information (ESI) available. CCDC 2401287, 2401032 and 2401036. For ESI and crystallographic data in CIF or other electronic format see DOI: https://doi.org/10.1039/d5se00195a

Open Access Article. Published on 30 2025. Downloaded on 29.11.2025 13:58:24.
This article is licensed under a Creative Commons Attribution-NonCommercial 3.0 Unported Licence.

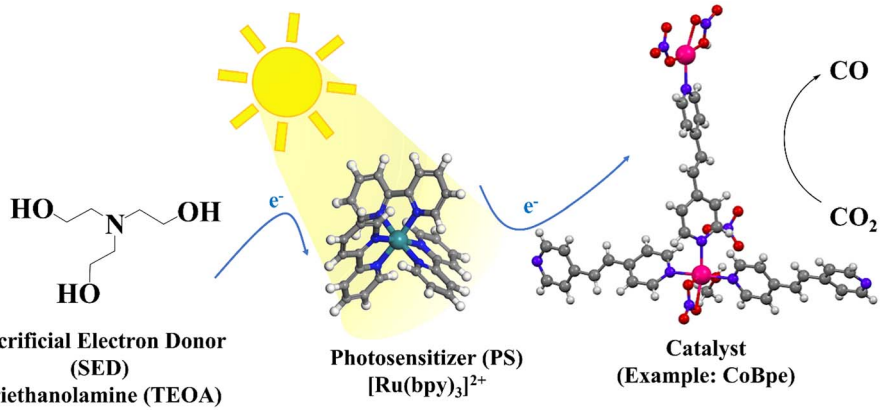

Fig. 1 Composition of the photocatalytic system used in this work for CO_2 reduction to CO – exemplified for **CoBpe**.

Organic Frameworks (MOFs),[33] and coordination polymers (CPs).[34–36] Most of these photocatalysts are involved in heterogeneous systems.[37] Additionally, homogeneous photocatalysis[38] (also known as a single-phase system, where all components are soluble in a one reaction medium) typically uses transition-metal complexes owing to their high solubility and metal center accessibility.[39]

Since the development of the square grid interpenetrated structure $[[Zn(bpy)_2(H_2O)_2]_nSiF_6]$ by Robson and Hoskins in 1990 [40] and Yaghi's creation of a 3D porous coordination polymer $[Cu(4,4'\text{-bpy})_{1.5}NO_3(H_2O)_{1.25}]$ in 1995,[41] coordination polymers (CPs) have been regarded as milestones in coordination chemistry. CPs are constructed by metal nodes connected through multidentate organic ligands forming infinite networks. They present remarkable properties and are employed in various fields (*e.g.*, drug delivery,[42] gas adsorption,[43] energy storage and separation,[44] photocatalysis[34]). The organic ligands used in CPs (*e.g.*, carboxylic acids,[45] oxalates,[46] pyridyls,[47] pyrazines[48]) exhibit diverse topologies, offering a wide range of coordination options. In addition, specific metal ions, including transition metals[49] and lanthanides,[50] are regarded as key components in the development and optimization of CP-based advanced materials due to their diverse chemical properties. Possessing suitable features (*e.g.*, semiconducting properties, metal cluster's availability,[51] structural tunability and adjustability, topological diversity, abundance of their electron-rich Lewis basic cores),[52,53] CPs have also attracted the scientific community's attention in the field of photocatalytic CO_2 reduction.

In this work, we successfully synthesized three coordination polymers (**CoBpe**, **NiBpe**, and **CuBpe**) based on the N-donor bridging ligand (1,2-di(4-pyridyl) ethylene, **Bpe**) and cobalt(II), nickel(II), and copper(II) transition metal ions, respectively. A similar structure has been published with cobalt(II),[54] while **NiBpe** and **CuBpe** are new compounds. The **Bpe** ligand[55] exists under two configurational isomers (*cis* and *trans*)[56] with the *trans*-configuration being more stable. This ligand is characterized by an electron-rich π-system,[57] a strong connectivity, and a high affinity for various metal cations including transition metals[58] and lanthanides.[59] These attributes offer a wide range of architectures and topologies for the resulting materials (*e.g.*, one-dimensional chains and ladders,[56,60] two-dimensional grids,[54] three-dimensional frameworks[61]). Thus, **Bpe** has been extensively employed in the development of 1D, 2D & 3D coordination polymers and Metal–Organic Frameworks exhibiting photoluminescence,[62] photocatalytic,[63–65] and gas adsorption properties.[66,67] Of note, a series of six CPs based on **Bpe** ligand and Co(II) metal cation have been developed by Peedikakkal and coworkers,[54] featuring interesting magnetic properties. The CPs reported herein (**CoBpe**, **NiBpe**, and **CuBpe**) were characterized using various techniques including CHN elemental analysis (EA), single crystal X-ray diffraction (SCXRD), powder X-ray diffraction (PXRD), infrared (IR) spectroscopy, and thermogravimetric analysis (TGA). In addition, solid-state UV-vis spectroscopy, linear sweep voltammetry (LSV), electrochemical impedance spectroscopy (EIS), and Mott–Schottky analysis were used to elucidate their photoelectrochemical properties. Furthermore, they were tested as catalysts for CO_2 photoreduction under simulated solar irradiation, in presence of $[Ru(bpy)_3]^{2+}$ as photosensitizer (PS) and triethanolamine (TEOA) as sacrificial electron donor (SED), proving their efficiency for CO production in such systems (Fig. 1).

Experimental

Chemicals

All chemical reagents and solvents employed were used without further purification. Details are provided in the ESI.†

Materials and methods

Single-crystal X-ray diffraction (SCXRD) data were collected for **CoBpe** at 100 K using a Rigaku Gemini diffractometer[68] equipped with a Rotating Anode source (Mo Kα radiation), a Rigaku Saturn 724+ CCD detector, and a kappa goniometer. For **NiBpe** and **CuBpe**, SCXRD data were collected at 150 K, using a Bruker Venture diffractometer equipped with a MetalJet source (Ga Kα radiation), a Helios MX optics, a Photon 100 CMOS detector, and a kappa goniometer. Crystal structure data collection, resolution and refinement were carried out using CrysAlisPro,[69,70] APEX,[71,72] OLEX2,[73,74] and SHELXL[75] crystallographic

 This journal is © The Royal Society of Chemistry 2025

Open Access Article. Published on 30 2025. Downloaded on 29.11.2025 13:58:24.
This article is licensed under a Creative Commons Attribution-NonCommercial 3.0 Unported Licence.

software packages. All non-hydrogen atoms were refined anisotropically with Least Squares minimization,[76] while hydrogen atoms were located and refined geometrically. Crystallographic data for **CoBpe**, **NiBpe**, and **CuBpe** have been deposited in the Cambridge Crystallographic Data Centre (CCDC) database under CCDC reference numbers 2401287, 2401032, and 2401036, respectively. Powder X-ray diffraction (PXRD) patterns were recorded from 5° to 50° using monochromatic CuKa radiation at room temperature. Calculated powder X-ray diffraction patterns were generated from the corresponding CIF files obtained from single-crystal analyses using Mercury software.[77] CHN analyses were performed on a Thermo Scientific FlashSmart instrument by the Elemental Analysis Service at Université de Montréal. FTIR spectra were measured using a Nicolet iS 10 Smart FT-IR spectrometer in the range from 4000 to 400 cm^{-1}. Thermogravimetric analysis (TGA) was performed using a PerkinElmer STA 6000 TGA/DTA apparatus in a range beginning from room temperature to 800 °C, under a N_2 gas flow, and using a heating rate of 10 °C min^{-1}. UV-visible absorption spectra were recorded in solid state using a UV-Visible Agilent Cary 60 spectrophotometer in the wavelength range of 200–800 nm. Photoelectrochemical characterization (linear sweep voltammetry (LSV), electrochemical impedance spectroscopy (EIS) and Mott–Schottky analysis) were performed using a three-electrode system (Autolab PGSTAT204) composed of a platinum net counter electrode, an Ag/AgCl reference electrode, and a sample-based working electrode fabricated by coating the coordination polymer samples (**CoBpe**, **NiBpe**, and **CuBpe**) on fluorine-doped tin-oxide (FTO) cells (2.5 cm × 5.0 cm), immersed in Na_2SO_4 electrolyte solution (0.1 M), pH 7. Photocatalytic CO_2 reduction experiments were performed in a 40 mL vial serving as a reactor vessel, using pre-dried coordination polymers (**CoBpe**, **NiBpe** and **CuBpe**) as catalysts and ($[Ru(bpy)_3]Cl_2 \cdot 6H_2O$ (bpy = 2′2-bipyridine)) as a photosensitizer. The reaction system was exposed to simulated sunlight with a power of 100 mW cm^{-2} (ABET SN103 Model 11.002 SunLite™ Solar Simulators equipped with a 150 W Xenon lamp). Further details are provided in the solar-light-driven CO_2 reduction section and the ESI.†

Synthetic procedures

CoBpe $[Co_2(Bpe)_3(NO_3)_4 \cdot MeOH]$. *Trans*-1,2-bis(4-pyridyl) ethylene (0.01 g, 0.054 mmol) and $Co(NO_3)_2 \cdot 6H_2O$ (0.1 g, 0.346 mmol) were dissolved in 7 mL of MeOH. A clear purple solution was obtained and placed in a 20 mL glass vial, which was sealed and kept undisturbed in an oven at 55 °C for 2 days. The solution was slowly cooled at room temperature. Pink crystals were extracted from the mother solution and washed with anhydrous MeOH. Yield: 70%. The crystals were suitable for X-ray diffraction. Anal. (%) calcd for $C_{37}H_{34}Co_2N_{10}O_{13}$: C, 47.05; H, 3.63; N, 14.83. Found: C, 46.52; H, 3.28; N, 14.77. FTIR (ATR, cm^{-1}): 3071(w), 2558(w), 1661(s), 1609(s), 1503(m), 1453(s), 1292(s), 1067(m), 806(m). UV-vis (solid-state) λ_{max}, nm: 267 (π–π*), 360 (shifted π–π*/MLCT), 507 (d–d).

NiBpe $[Ni_2(Bpe)_3(NO_3)_4 \cdot MeOH]$. *Trans*-1,2-bis(4-pyridyl) ethylene (0.01 g, 0.054 mmol) and $Ni(NO_3)_2 \cdot 6H_2O$ (0.1 g, 0.346 mmol) were dissolved in 7 mL of MeOH. A clear green solution was obtained and placed in a 20 mL glass vial, which was sealed and kept undisturbed in an oven at 65 °C for 2 days. The solution was slowly cooled at room temperature. Green crystals were extracted from the mother solution and washed with anhydrous MeOH. Yield: 65%. The crystals were suitable for X-ray diffraction. Anal. (%) calcd for $(C_{37}H_{34}Ni_2N_{10}O_{13})(H_2O)$: C, 46.19; H, 3.77; N, 14.56. Found: C, 46.07; H, 3.48; N, 14.62. FTIR (ATR, cm^{-1}): 3288(w), 2980(w), 1657(s), 1605(s), 1506(m), 1420(s), 1263(s), 1075(m), 835(m). UV-vis (solid-state) λ_{max}, nm: 268 (π–π*), 355 (shifted π–π*/MLCT), 612 (d–d).

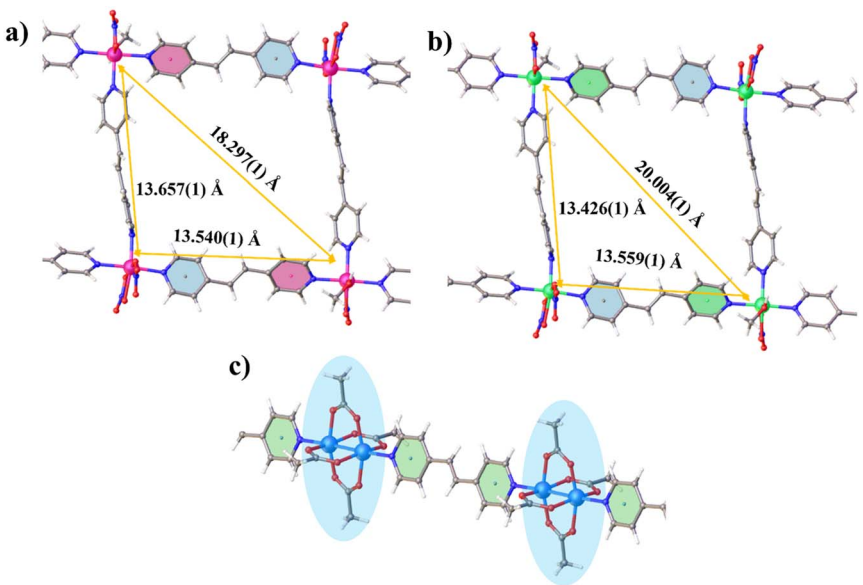

Fig. 2 The solid-state structures of **CoBpe** (a) and **NiBpe** (b), featuring a square grid coordination mode, and **CuBpe** (c), highlighting a 1D linear chain topology with the classic paddle-wheel coordination mode of copper centers.

Open Access Article. Published on 30 2025. Downloaded on 29.11.2025 13:58:24.
This article is licensed under a Creative Commons Attribution-NonCommercial 3.0 Unported Licence.

CuBpe $[Cu(CH_3COO)_2(Bpe)_{0.5}]$. *Trans*-1,2-bis(4-pyridyl) ethylene (0.01 g, 0.054 mmol) and $Cu(CH_3COO)_2$ (0.062 g, 0.346 mmol) were dissolved in a mixture of solvents DMF/MeOH (7 mL, 5 : 2 v/v) in a 20 mL glass vial, which was sealed and kept undisturbed in an oven at 85 °C for 2 days. The solution was slowly cooled at room temperature. Blue crystals were obtained, extracted from the mother solution and washed with anhydrous MeOH. Yield: 100%. The crystals were suitable for X-ray diffraction. Anal. (%) calcd for $(C_{10}H_{11}CuNO_4)(H_2O)_{0.5}$ C, 42.63; H, 4.29; N, 4.97. Found: C, 42.80; H, 4.21; N, 5.17. FTIR (ATR, cm^{-1}): 3288(w), 3058(w), 2155(s), 1630(s), 1349(m), 1263(s), 1225(s), 1014(m), 678(m). λ_{max}, nm: 252 (π–π*), 388 (shifted π–π*/MLCT), 700 (d–d).

Results and discussion

CoBpe, **NiBpe**, and **CuBpe** were synthesized in good yields, as air-stable crystals, by reacting the metal salt of corresponding cation (Co(II), Ni(II), and Cu(II), respectively), with the organic ligand 1,2-di(4-pyridyl) ethylene (**Bpe**), under solvothermal conditions. CHN elemental analysis and powder X-ray diffraction analysis (PXRD) were used to confirm their purity (in bulk). Full details on these syntheses and characterization are given in the Experimental section and ESI.†

XRD-single crystal solid-state structures were determined for each of the three CPs (Fig. 2 and S1–S3, ESI†). Crystal data and structure refinement details are given in Table S1† and the values for bond lengths, angles, and the H-bonding geometry are provided in Tables S2–S9.† The isostructurality of **CoBpe** and **NiBpe** was confirmed by SCXRD analysis. Both compounds crystallize in a monoclinic system and a $P2_1/c$ space group, showing a 1D ladder structure with interpenetrated square grids (Fig. 2). The asymmetric unit contains two independent metal centers (Fig. S1–S3†), each hexacoordinated and adopting a distorted octahedral geometry with an "MN_3O_3" coordination sphere. The first metal center is coordinated to three nitrogen atoms from three **Bpe** ligands (two axial, one equatorial) forming a T-shape geometry. Additionally, the metal center is coordinated by one oxygen atom from the solvent molecule (methanol) and two oxygen atoms from nitrate anions in a bidentate manner. Similarly, the second metal center is coordinated to three **Bpe** ligands in a T-shape topology, neighbored by two nitrate molecules coordinated in bidentate and monodentate manners. These arrangements repeat infinitely, resulting in a square-grid structure that creates 1D ladder networks. Each square is formed by four parallel **Bpe** ligands and four metal centers occupying the square grid vertices. The distances between metal centers are 13.657(1) Å and 13.540(1) Å for **CoBpe**, and 13.426(1) Å and 13.559(1) Å for **NiBpe**. These grids intersect with those from neighboring ladders; each square grid is interpenetrated with two ladders, creating a 3D interpenetrated network (Fig. S4†). Furthermore, the ethene link (–CH = CH–) in the **Bpe** ligand structure disrupts the coplanarity of pyridine rings, as C–H moieties of the adjacent **Bpe** ligands sterically clash.[78] The non-planarity is essential to accommodate the three pyridyl donors at the T-shaped metal centers, reducing steric repulsion and promoting efficient packing in the overall structure.

CuBpe crystallizes in a triclinic system and a *P*-1 space group. Its asymmetric unit consists of a paddlewheel copper acetate dimer $[Cu_2(OAC)_4]$ axially coordinated to coplanar **Bpe** ligands (Fig. S3†). Thus, each Cu(II) center in the dimer is coordinated to four oxygen atoms belonging to four bridging acetate ligands and one nitrogen atom from the **Bpe** ligands (Fig. 2c and S5†). The extended structure results in 1D channels defined by the paddlewheel copper cluster $[Cu_2(OAC)_4(Bpe)_2]$.[79] This arrangement repeats infinitely, forming alternating 2D layers (Fig. S5†). The Co–O and Co–N coordination bond lengths in **CoBpe** are as following: [2.0380(15)–2.2314(14)] Å and [2.1531(15)–2.1026(15)] Å, respectively, while for **NiBpe**, the Ni–O and Ni–N bond lengths are [2.0262(14)–2.1704(13)] Å and [2.0639(13)–2.0999(14)] Å. These measurements align with those previously reported.[80] The intermetallic distance in the dinuclear copper cluster is 2.6182(5) Å, while Cu–O and Cu–N bond lengths are [1.964(10)–1.985(9)] Å and [2.16(2)–2.18(3)] Å, respectively. These results are in good agreement with those found for the

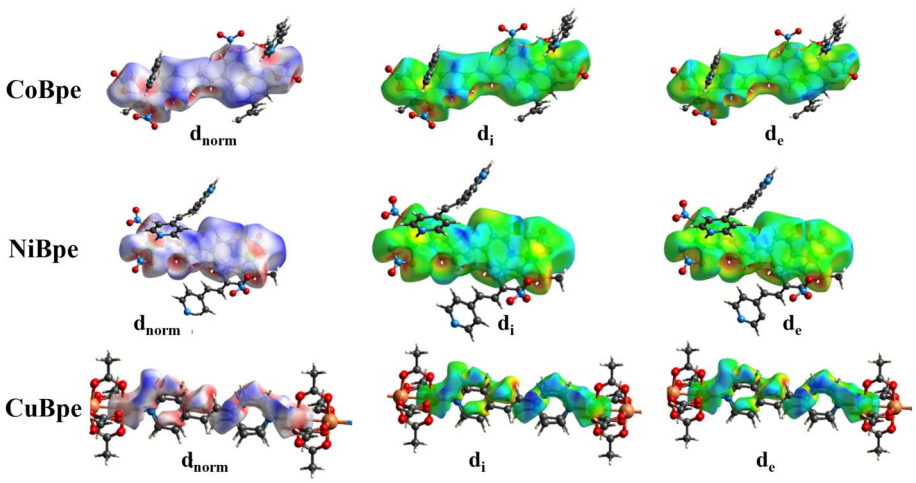

Fig. 3 View of Hirshfeld surfaces of **CoBpe**, **NiBpe**, and **CuBpe** with their normalized contact distances d_{norm}, d_i, and d_e.

 This journal is © The Royal Society of Chemistry 2025

Open Access Article. Published on 30 2025. Downloaded on 29.11.2025 13:58:24.
This article is licensed under a Creative Commons Attribution-NonCommercial 3.0 Unported Licence.

dinuclear cupric acetate $Cu_2(CH_3COO)_4(H_2O)_2$, as determined by Hull in 1938.[81,82] The bulk purity of 'as-synthesized' compounds was verified by powder X-ray diffraction analysis (PXRD). Collected patterns match well with simulated ones, particularly for the major peak positions, confirming the purity of the compounds and the presence of a single crystalline phase (Fig. S6†).

Hirshfeld surface analysis (HS) was conducted using CrystalExplorer software[83] in order to further explore the intermolecular and surface interactions between neighboring molecules within the crystal lattice. The normalized contact distance (d_{norm}) is presented using a color code: white, blue and red. These colors highlight the interactions between neighboring atoms. Red spots indicate closer atomic contacts, blue spots represent longer contacts and white areas correspond to the van der Waals interactions. In this analysis, d_e denotes the distance measured from the surface to the nearest external nucleus, while d_i is the distance from the surface to the nearest internal nucleus. The red spots observed on the d_{norm} surface (Fig. 3) are predominantly located around the metal center, showing regions of strong contact interactions. The 2D fingerprint plots (Fig. S7 and S8†) reveal the contribution of hydrogen interactions, highlighting the predominance of hydrogen bonding within the structures.

FTIR spectra (Fig. 4a) of these materials exhibited a weak signal around 3000–3100 cm^{-1} attributed to ν(C–H) stretching vibration from the aromatic pyridine ring, a strong signal within 1400–1600 cm^{-1} range corresponding to the characteristic stretching vibration ν(C=C) of the pyridine, and a medium signal positioned in the interval 1350–1000 cm^{-1} belonging to the ν(C–N) stretching vibration. In addition, the characteristic signal related to the ν(C=C) stretching vibration of the ethylene bridging spacer is observed in the 1680–1600 cm^{-1} range. Notable similarity of the CPs FTIR spectra is found when compared to that of the free ligand (**Bpe**), with changes in the fingerprint region below 1500 cm^{-1}. These changes are due to the coordination bond formed between the N-donor atom of **Bpe** and the transition metal centers, typically observed around 400–600 cm^{-1} (Fig. 4a).

Thermal stability of the CPs reported herein was evaluated by thermogravimetric analysis (TGA) in a temperature range of 30 °C to 800 °C (Fig. 4b). **CoBpe** showed a first weight loss at 78 °C, corresponding to the release of methanol solvent, followed by a second significant weight loss near 275 °C, which marked the decomposition of the coordination polymer lattice. **NiBpe** also exhibited two weight loss phenomena, the first one at 88 °C related to the departure of methanol according to the crystalline structure, and the second one at 350 °C corresponding to the degradation of the polymer. **CuBpe** is stable up to 265 °C, showing no solvent loss, in line with its XRD structure. The decomposition temperature at 95% (T_d (95%)) was evaluated to be 304 °C for **CoBpe**, 354 °C for **NiBpe** and 291 °C for **CuBpe**, confirming their excellent thermal stability (Fig. 4b).

Solid-state UV/vis absorption spectroscopy was conducted in the region 200–800 nm (Fig. 4c). All compounds (**Bpe** ligand and CPs) display an absorption band in the UV region between 250

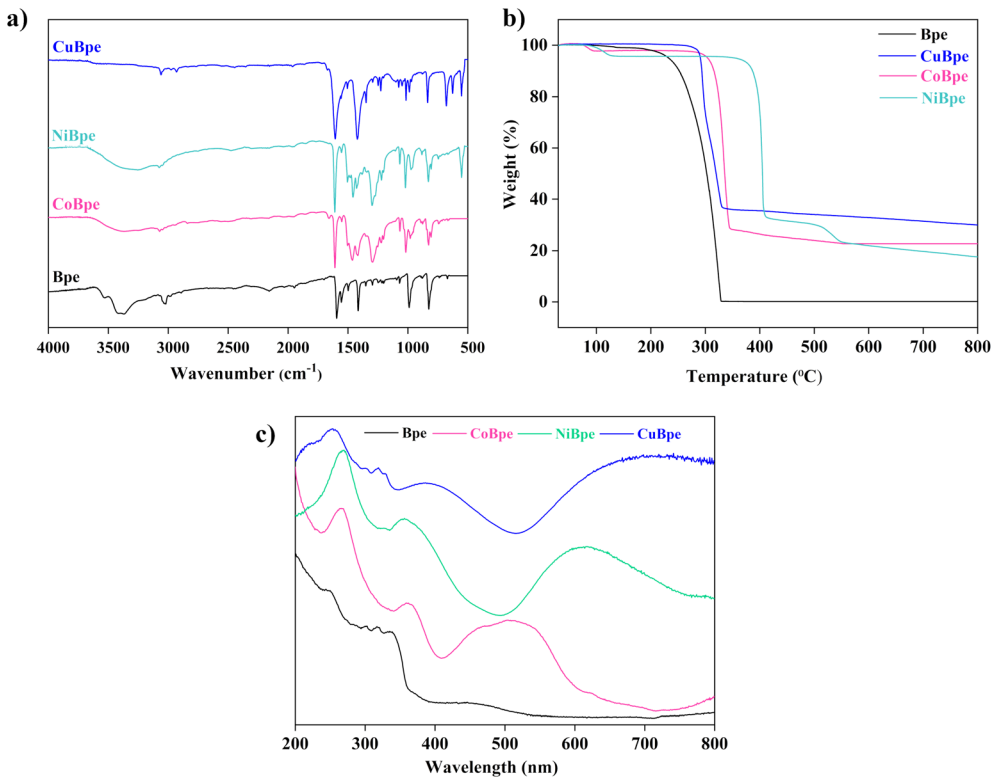

Fig. 4 (a) FTIR-ATR spectra, (b) TGA curves, and (c) UV-vis absorption spectra in solid state of **Bpe** (black), **CoBpe** (pink), **NiBpe** (green) and **CuBpe** (blue).

Open Access Article. Published on 30 2025. Downloaded on 29.11.2025 13:58:24.
This article is licensed under a Creative Commons Attribution-NonCommercial 3.0 Unported Licence.

and 350 nm, corresponding to π–π* transitions within the **Bpe** aromatic and conjugated system.[84] The CPs exhibit a broad absorption band in the near UV, centered around 360–380 nm assigned to shifted π–π* transitions, due to complexation and/or metal to ligand charge transfer (MLCT) transitions (electron transfer from a d-orbital of the metal center to ligand orbitals). The large band in the visible region (450–800 nm: 507 nm for **CoBpe**, 612 nm for **NiBpe**, and 700 nm for **CuBpe**) is assigned to d–d (metal-centered) transitions. As a general feature, the absorption bands are significantly red-shifted in the CPs *vs.* the **Bpe** ligand due to the coordination of the transition metal ions (Co(II), Ni(II), Cu(II)) to the latter.

To better assess the electronic properties of the CPs, their bandgap energy was calculated using Tauc plot method[85] (Fig. S10†). **CuBpe** shows the lowest bandgap energy of 1.10 eV, while **CoBpe** and **NiBpe** exhibit 1.86 eV and 1.60 eV, respectively, highlighting their semiconducting characteristics. Bardeen, Shockley, and Brattain initiated the discovery of semiconductors in 1948.[86] Their contributions shifted the scientific community's interest toward the electronic properties of the materials, including optical and photochemical aspects, and have paved the way for the development of modern electronic devices.[87]

Photoelectrochemical properties of the compounds were also investigated using various techniques: linear sweep voltammetry (LSV), electrochemical impedance spectroscopy (EIS), and Mott–Schottky analysis. Prior to LSV measurements, an anodic scan (Fig. S11†) was performed by linearly varying the applied potential from negative to positive values (−0.1 V to 1.1 V) and measuring the resulting current. **CoBpe** exhibited a high onset potential of 0.44 V and it also showed a resulting current of 4.98 μA at 1.0 V. This value is significantly lower compared to those obtained for **Bpe** and **NiBpe**, which displayed onset potentials of 0.08 V and 0.41 V, respectively, and a resulting current of 94.66 μA and 57.61 μA at 1.0 V. Moreover, **CuBpe** had an onset potential value of 0.34 V with a high current response of 178.08 μA at 1.0 V. The high onset potential observed for **CoBpe** suggests efficient separation of electron–hole pairs before recombination and facile promotion of electronic conduction in the system. These observations support its better performance for CO_2 reduction reactions (*vide infra*). Both the onset potential and current response suggest that **CuBpe** is the most responsive compared to the other CPs herein and are indicative of its high conductivity.[88] These properties can be attributed to the availability of electrons on its surface, in line with its structure (metallic dimers in **CuBpe** *versus* mononuclear coordination moieties in **CoBpe** and **NiBpe**). These results confirmed that the materials herein are typical n-type semiconductors, displaying interesting properties toward electrochemical separation and transfer of charge carriers (electrons) from the valence band (VB) to the conduction band (CB). EIS measurements delve into the phenomena of charge transfer resistance occurring on the surface of materials. Nyquist plots (Fig. S12†) can appear as semi-circle arcs or linear lines called Warburg tails, giving information about the impedance behavior of the system.[89] The Nyquist plots exhibit the largest semi-arc for **Bpe**, followed by **NiBpe**, and **CuBpe**. In contrast, **CoBpe** shows the smallest semi-arc, indicating the presence of an ohmic interface with low electrical resistance. This behavior confirms its high conductivity and facile charge transfer. Mott–Schottky (MS) analysis was also performed to estimate the conduction band (CB) positions by determining the flat-band potential (E_{fb}) of the CPs.[87] The measurements were taken at 2500 Hz, and the MS plots showed positive slopes, characteristic of n-type semiconductors.[90] Thus, the conduction band potential is estimated to be more negative by approximately 0.1 V than the flat-band potential.[90,91] From Fig. S13,† the E_{fb} values were estimated to be −1.29 V for **CoBpe**, −0.87 V for **NiBpe**, and −1.00 V for **CuBpe** (*vs.* Ag/AgCl) or −1.09 V, −0.67 V, and −0.80 V *vs.* the Normal Hydrogen Electrode (NHE). The corresponding conduction band potentials (LUMO levels) are calculated to be −1.19 V, −0.77 V, and −0.90 V (*vs.* NHE), respectively (Fig. 5 and S14†). Furthermore, the energy bandgap values (calculated by Tauc plot method) were used to determine the

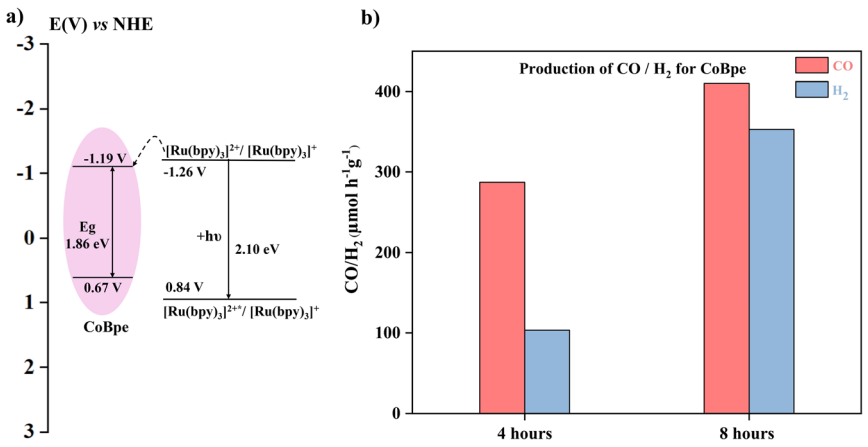

Fig. 5 (a) Electron-transfer diagram for **CoBpe**.[93] (b) Photocatalytic CO and H_2 production using **CoBpe** as catalyst (10 mg) under simulated solar irradiation for 4 hours and 8 hours; $[Ru(bpy)_3]Cl_2 \cdot 6H_2O$ (7.4 mg) added as photosensitizer; MeCN/H_2O/TEOA (3/1/1, 10 mL). Experiments were performed at least in duplicate, and the error (1–15%) represents the standard deviation for repeated measurements.

 This journal is © The Royal Society of Chemistry 2025

Open Access Article. Published on 30 2025. Downloaded on 29.11.2025 13:58:24.
This article is licensed under a Creative Commons Attribution-NonCommercial 3.0 Unported Licence.

HOMO levels of the CPs, employing the formula: $E_{VB} = E_g + E_{CB}$, where E_{VB} is the potential of the valence band, E_{CB} is the potential of the conduction band, and E_g is the energy gap.[92] Thus, valence band potentials (HOMO levels) of 0.67 V, 0.83 V, and 0.20 V were obtained for **CoBpe**, **NiBpe** and **CuBpe**, respectively.

The LUMO level values of the three CPs are more negative than the reduction potential of CO_2/CO (−0.53 V *vs.* NHE), suggesting that these materials can be used as catalysts for CO_2 reduction into CO. In addition, the CB/LUMO potentials of all three CPs are less negative than that of the classical photosensitizer $[Ru(bpy)_3]^{2+}$ ($(E_{1/2}[Ru(bpy)_3]^{2+}/[Ru(bpy)_3]^{+}) = -1.26$ V *vs.* NHE),[93] indicating favorable photoinduced electron transfer (from the reduced photosensitizer to the CB of the CPs), a key step in photocatalytic processes. Charge transfer diagrams are illustrated in Fig. 5a and S14.†

Based on the absorption features observed in the visible region and the previously elucidated optical and photoelectrochemical properties, the solar-light-driven CO_2 reduction photocatalytic activity was studied for the CPs reported herein. To determine optimal experimental conditions and gain insights into the photocatalytic mechanism, various control experiments were performed (Table S10†). First, the mass of the catalyst was varied (2.5, 5, and 10 mg) under identical reaction conditions (4 hours of continuous simulated solar irradiation). The results revealed that when using 5 mg and 10 mg of catalyst, high CO production rates, and good selectivity of CO *vs.* H_2 generation are obtained (Fig. S16 and S17†). At a catalyst mass of 10 mg, the CO production is slightly lower than that obtained using 5 mg of catalyst, while selectivity toward CO is enhanced (Table S10†). The lower activity at higher catalyst loadings could be explained by the fact that charge recombination is more significant, leading to a less efficient reaction. In the same time, a higher catalyst concentration increases the number of active sites, which can modify the adsorption and binding of reactants and intermediates, with impact on selectivity, in this case favoring CO_2 over proton reduction. The higher catalyst amount also helps stabilize reactive intermediates and minimizes the formation of undesirable species that can impact selectivity. These considerations could explain the observed shift in CO/H_2 selectivity when using different catalyst loadings. Taken together, these factors make 10 mg the optimal catalyst mass for maximizing CO production while minimizing unwanted side reactions, justifying its selection for further studies. As a result, the catalyst mass was fixed at 10 mg for the subsequent experiments (Table S10†).

CoBpe produced 287 μmol g^{-1} h^{-1} of CO with a selectivity of 74%, whereas **NiBpe** produced only 33 μmol g^{-1} h^{-1} of CO under the same conditions, and **CuBpe** showed no activity. The free **Bpe** ligand and metal salts were also evaluated. Using **Bpe** as a catalyst showed a CO production rate of 91 μmol g^{-1} h^{-1} (Table S10†). However, this performance remains much lower than that obtained using **CoBpe**. The use of cobalt salt showed a low CO production rate of 45 μmol g^{-1} h^{-1}. H_2 (110 μmol g^{-1} h^{-1}) was also produced in the latter experiment. Furthermore, none of the nickel and copper salts exhibited photocatalytic activity under the same conditions. These tests confirmed the efficiency of Co(II) as an active site for CO_2 photoreduction.[94] Moreover, running the reaction in the absence of catalyst results in no activity for CO_2 reduction. The same response (no activity) is obtained while excluding the photosensitizer or conducting the reaction in the absence of light irradiation. Based on these results, **CoBpe**, **NiBpe**, and **CuBpe** cannot be classified as independent photocatalysts, since they are unable to initiate CO_2 photoreduction in the absence of photosensitizer. Therefore, these materials are considered to function only as catalysts in the type of photocatalytic system under study here. The reaction medium (MeCN/H_2O mixture) and sacrificial electron donor (SED) type (triethanolamine (TEOA)) and their ratio (MeCN/H_2O/TEOA (3/1/1)) were selected based on similar photocatalytic systems for CO_2 reduction already published.[94] It was found that this choice of solvents/SED has a synergy impact when combined with the photosensitizer, the catalyst, and the CO_2 gas, as removing one of the solvents/SED components significantly affected the CO production rate. It is also important to note that purging the reaction with Ar gas instead of CO_2 gas revealed no photocatalytic activity for CO_2 reduction, while 177 μmol g^{-1} h^{-1} of H_2 were produced, under the same conditions, proving that **CoBpe** can serve as an active catalyst for proton reduction (Table S12†). In addition, the same experiment confirms the evolution of CO from CO_2 gas and not from any other sources, such as solvents or degradation of organic compounds. Furthermore, the influence of the reaction time was also assessed (Fig. 5b): after 8 hours of irradiation, despite a loss in selectivity, the CO production rate for **CoBpe** reached 410 μmol g^{-1} h^{-1}, an increase by 1.4 times *vs.* that obtained for the 4-hour experiment. These results are in line with the published data for similar reaction conditions (Table S11†).[61]

The better performance of **CoBpe** for CO_2 photoreduction among the three CPs studied herein (Fig. S16 and S17†) can be explained by its photoelectrochemical properties (*vide supra*). Charge-separation efficiency is crucial for effective CO_2 photoreduction. According to LSV measurements, **CoBpe** exhibits the highest onset potential, suggesting its capacity for more efficient separation of electron–hole pairs compared to **NiBpe** and **CuBpe**. This observation is further supported by EIS measurements, where **CoBpe** exhibits the smallest semi-arc, corresponding to the lowest charge transportation resistance. Thus, these properties of **CoBpe** translate into its highest CO_2 reduction activity within the studied CPs series.

Based on the electron–transfer diagrams of the compounds under study (Fig. 5a and S14†), the control experiments performed in this work, and previous published results on similar research projects,[61,90,94–97] the following mechanism is proposed for the light driven photoreduction of CO_2 to CO in the systems investigated herein. Upon simulated solar irradiation, the photosensitizer (PS) $[Ru(bpy)_3]^{2+}$ reaches its excited state ($(E_{1/2}[Ru(bpy)_3]^{2+*}/[Ru(bpy)_3]^{+}) = 0.84$ V *vs.* NHE),[93] and can receive an electron from the sacrificial electron donor (TEOA; E_{ox} = +0.89 V *vs.* NHE in MeCN and +1.10 V *vs.* NHE in water).[98,99] Subsequently, the reduced PS, $[Ru(bpy)_3]^{+}$ ($(E_{1/2}[Ru(bpy)_3]^{2+}/[Ru(bpy)_3]^{+}) = -1.26$ V *vs.* NHE),[93] will reform the initial $[Ru(bpy)_3]^{2+}$ species, by transferring an electron to the

Open Access Article. Published on 30 2025. Downloaded on 29.11.2025 13:58:24.
This article is licensed under a Creative Commons Attribution-NonCommercial 3.0 Unported Licence.

conduction band/LUMO level of the CP acting as catalyst. The CB/LUMO potentials of the three CPs are less negative than ($(E_{1/2}[Ru(bpy)_3]^{2+}/[Ru(bpy)_3]^{+}) = -1.26$ V *vs.* NHE).[93] Furthermore, at the CP/catalyst level, the CB/LUMO potentials for all CPs in this study are more negative than the CO_2/CO reduction potential (−0.53 V *vs.* NHE), enabling their activity for CO_2 reduction. Thus, the electrons photoinjected on the surface of the catalyst will reduce the metallic sites to their active catalytic forms, which bind CO_2. For **CoBpe**, the Co(II) centers (d^7, with a distorted octahedral geometry) are reduced to low-valent Co(I) d^8 species. These species act as the active catalytic sites for CO_2 binding. They display a tetra-coordinated square planar geometry, favored on electronic grounds; the existence of penta-coordinated trigonal bipyramidal or square pyramidal intermediates is also possible.[100] To achieve these geometries, the labile ligands coordinated to the metal center, such as solvent molecules and coordinated nitrate ions dissociate. A detailed proposal of these structural changes, based on the information highlighted by the solid-state structure of **CoBpe** is given in Fig. S18.† The metal ion – CO_2 adducts will further undergo the following subsequent steps: proton transfer, proton-coupled electron transfer (PCET)[101] and loss of a water molecule, to form CO, which is released as gas.[61,90,95–97,101] The detailed proposed catalytic cycle, exemplified for **CoBpe**, is presented in Fig. S18.†

Conclusion

To sum up, three coordination polymers (**CoBpe**, **NiBpe**, and **CuBpe**) based on transition metal ions (Co(II), Ni(II), Cu(II)) and a bis(pyridyl) ligand (**Bpe**, 1,2-di(4-pyridyl)ethylene) were successfully synthesized and characterized. Single-crystal X-ray diffraction revealed that **CoBpe** and **NiBpe**, are isostructural, crystallizing in a monoclinic system and a $P2_1/c$ space group, while **CuBpe** crystallizes in a triclinic system and a $P\text{-}1$ space group. **CoBpe** and **NiBpe** adopted a 1D ladder structure with interpenetrated square grids forming a 3D network, whereas **CuBpe** formed a 1D channel packed on 2D alternating layers. These structural differences are attributed to variations in counter anions and experimental conditions. These functional materials exhibit interesting optical and photoelectrochemical properties and present notable photocatalytic activity toward CO_2 reduction into CO, a promising new-generation feedstock fuel. **CoBpe** demonstrated a high CO production rate of 287 μmol g^{-1} h^{-1} (4-hour experiment) and 410 μmol g^{-1} h^{-1} (8-hour experiment) under continuous simulated sunlight. These results are competitive when compared to those currently published, obtained under similar conditions. Beyond the quantified performance of CPs used as catalysts for CO_2 photoreduction, this study offers further insights into the structure–properties–reactivity relation in photocatalytic systems based on CPs. Due to their chemical and thermal stability, along with semiconducting and photoelectrochemical properties, the materials herein demonstrate the great potential that CPs have as catalysts for CO_2 photoreduction, paving the way toward sustainable green energy development. Moreover, their photoelectrochemical properties suggest them as possible candidates for application in various other areas (*e.g.*, dye degradation, photoredox chemistry, optoelectronic devices).

Data availability

The data supporting this article have been included in the main manuscript (Fig. 1–5) and as part of the ESI.† Crystallographic data for compounds **CoBpe**, **NiBpe** and **CuBpe** has been deposited at the CCDC under following accession numbers: 2401287, 2401032 and 2401036, respectively.

Author contributions

Conceptualization: A. A.; supervision and funding: M. C. & S. B.; investigation and methodology: A. A., M. C.; synthesis and characterization: A. A.; crystal structures: D. C. & M. E.; photocatalysis and electrochemical characterization: A. Q., A. A. & T. O. D.; writing original draft: A. A., M. C. & S. B.; revision: A. A., M. C., S. B., M. E., A. Q. & T. O. D.

Conflicts of interest

The authors declare no competing financial interest.

Acknowledgements

We are grateful to the Natural Sciences and Engineering Research Council of Canada (NSERC), the Canadian Foundation for Innovation (CFI), Mitacs, the Québec Center for Advanced Materials (QCAM), le Réseau québécois de l'énergie intelligente (RQEI), the Institut d'Innovations en Ecomatériaux Écoproduits et Ecoénergies (I2E3), the Institut de Recherche sur l'Hydrogène (IRH), and the Université du Québec à Trois-Rivières (UQTR) for financial support. We also thank the Biochemistry, Chemistry, Physics, and Forensic Science Department of UQTR, the Chemical Engineering Department of Université de Laval, and the Chemistry Department of Université de Montréal for access to the research platforms.

References

1 R. Quadrelli and S. Peterson, *Energy Policy*, 2007, **35**, 5938–5952.
2 L. Zeng, X. Guo, C. He and C. Duan, *ACS Catal.*, 2016, **6**, 7935–7947.
3 R. Gross, M. Leach and A. Bauen, *Environ. Int.*, 2003, **29**, 105–122.
4 F. Bowen, *Energy Policy*, 2011, **39**, 2256–2264.
5 S. Xie, Q. Zhang, G. Liu and Y. Wang, *Chem. Commun.*, 2016, **52**, 35–59.
6 B. Kumar, M. Llorente, J. Froehlich, T. Dang, A. Sathrum and C. P. Kubiak, *Annu. Rev. Phys. Chem.*, 2012, **63**, 541–569.
7 B. Wu, Y. Gao, F. Jin, J. Cao, Y. Du and Y. Zhang, *Catal. Today*, 2009, **148**, 405–410.
8 M. Arsalan, D. Ewis, N. Mahmud, M. M. Ba-Abbad, M. Khaled and M. H. El-Naas, *J. Environ. Chem. Eng.*, 2023, **11**, 111352.

 This journal is © The Royal Society of Chemistry 2025

Open Access Article. Published on 30 2025. Downloaded on 29.11.2025 13:58:24.
This article is licensed under a Creative Commons Attribution-NonCommercial 3.0 Unported Licence.

9 R. Bhardwaj, T. Sharma, D. D. Nguyen, C. K. Cheng, S. S. Lam, C. Xia and A. K. Nadda, *J. Environ. Manage.*, 2021, **289**, 112468.
10 C.-Y. Chou and R. F. Lobo, *Appl. Catal., A*, 2019, **583**, 117144.
11 S. J. Park, M. P. Bukhovko and C. W. Jones, *Chem. Eng. J.*, 2021, **420**, 130369.
12 J. He and C. Janaky, *ACS Energy Lett.*, 2020, **5**, 1996–2014.
13 R. Napier, B. Roldan Cuenya and M. Koper, *J. Phys. D:Appl. Phys.*, 2022, **55**, 42–43.
14 H. L. Tuller, *Materials for Renewable and Sustainable Energy*, 2017, vol. 6, pp. 1–16.
15 A. Harriman, *Philos. Trans. R. Soc., A*, 2013, **371**, 20110415.
16 G. Segev, J. Kibsgaard, C. Hahn, Z. J. Xu, T. G. Deutsch, C. Xiang, J. Z. Zhang, L. Hammarström, D. G. Nocera and A. Z. Weber, *J. Phys. D: Appl. Phys.*, 2022, **55**, 323003.
17 R. Ameta, M. S. Solanki, S. Benjamin and S. C. Ameta, in *Advanced Oxidation Processes for Waste Water Treatment*, Elsevier, 2018, pp. 135–175.
18 F. E. Osterloh, *ACS Energy Lett.*, 2017, **2**, 445–453.
19 X. Yang and D. Wang, *ACS Appl. Energy Mater.*, 2018, **1**, 6657–6693.
20 H. Honda, A. Ishizaki, R. Soma, K. Hashimoto and A. Fujishima, *J. Illum. Eng. Soc.*, 1998, **27**, 42–49.
21 K. Saeed, I. Khan, T. Gul and M. Sadiq, *Appl. Water Sci.*, 2017, **7**, 3841–3848.
22 A. Houas, H. Lachheb, M. Ksibi, E. Elaloui, C. Guillard and J.-M. Herrmann, *Appl. Catal., B*, 2001, **31**, 145–157.
23 N. Alahmadi, *Separations*, 2022, **9**, 264.
24 V. Seiß, S. Thiel and M. Eichelbaum, *Inorganics*, 2022, **10**, 139.
25 J. Bedia, V. Muelas-Ramos, M. Peñas-Garzón, A. Gómez-Avilés, J. J. Rodríguez and C. Belver, *Catalysts*, 2019, **9**, 52.
26 K. Li, B. Peng and T. Peng, *ACS Catal.*, 2016, **6**, 7485–7527.
27 A. Mills and S. Le Hunte, *J. Photochem. Photobiol., A*, 1997, **108**, 1–35.
28 M. Batzill, *Energy Environ. Sci.*, 2011, **4**, 3275–3286.
29 S. Zhang, X. Ou, Q. Xiang, S. A. Carabineiro, J. Fan and K. Lv, *Chemosphere*, 2022, **303**, 135085.
30 Z. Cheng, W. Qi, C. H. Pang, T. Thomas, T. Wu, S. Liu and M. Yang, *Adv. Funct. Mater.*, 2021, **31**, 2100553.
31 H. Mai, D. Chen, Y. Tachibana, H. Suzuki, R. Abe and R. A. Caruso, *Chem. Soc. Rev.*, 2021, **50**, 13692–13729.
32 Y. Yuan, R.-t. Guo, L.-f. Hong, X.-y. Ji, Z.-d. Lin, Z.-s. Li and W.-g. Pan, *Mater. Today Energy*, 2021, **21**, 100829.
33 H. Wang, H. Wang, Z. Wang, L. Tang, G. Zeng, P. Xu, M. Chen, T. Xiong, C. Zhou and X. Li, *Chem. Soc. Rev.*, 2020, **49**, 4135–4165.
34 H. Zhang, G. Liu, L. Shi, H. Liu, T. Wang and J. Ye, *Nano energy*, 2016, **22**, 149–168.
35 Y. Wu, L. Lu, J. Feng, Y. Li, Y. Sun and A. Ma, *J. Solid State Chem.*, 2017, **245**, 213–218.
36 A. Kuila, N. A. Surib, N. S. Mishra, A. Nawaz, K. H. Leong, L. C. Sim, P. Saravanan and S. Ibrahim, *ChemistrySelect*, 2017, **2**, 6163–6177.
37 S. Gisbertz and B. Pieber, *ChemPhotoChem*, 2020, **4**, 456–475.
38 I. Arslan-Alaton, *Dyes Pigm.*, 2004, **60**, 167–176.
39 H. Hennig, *Coord. Chem. Rev.*, 1999, **182**, 101–123.
40 B. F. Hoskins and R. Robson, *J. Am. Chem. Soc.*, 1990, **112**, 1546–1554.
41 O. M. Yaghi, H. Li, C. Davis, D. Richardson and T. L. Groy, *Acc. Chem. Res.*, 1998, **31**, 474–484.
42 Z. Ma and B. Moulton, *Coord. Chem. Rev.*, 2011, **255**, 1623–1641.
43 T. Ghanbari, F. Abnisa and W. M. A. W. Daud, *Sci. Total Environ.*, 2020, **707**, 135090.
44 H. Li, K. Wang, Y. Sun, C. T. Lollar, J. Li and H.-C. Zhou, *Mater. Today*, 2018, **21**, 108–121.
45 Y. Han, X. Li, L. Li, C. Ma, Z. Shen, Y. Song and X. You, *Inorg. Chem.*, 2010, **49**, 10781–10787.
46 P. Thuéry and E. Rivière, *Dalton Trans.*, 2013, **42**, 10551–10558.
47 S. R. Batten, J. C. Jeffery and M. D. Ward, *Inorg. Chim. Acta*, 1999, **292**, 231–237.
48 J. Lu, T. Paliwala, S. C. Lim, C. Yu, T. Niu and A. J. Jacobson, *Inorg. Chem.*, 1997, **36**, 923–929.
49 B. Moulton and M. J. Zaworotko, *Curr. Opin. Solid State Mater. Sci.*, 2002, **6**, 117–123.
50 J. Heine and K. Müller-Buschbaum, *Chem. Soc. Rev.*, 2013, **42**, 9232–9242.
51 D. Sun, Y. Fu, W. Liu, L. Ye, D. Wang, L. Yang, X. Fu and Z. Li, *Chem.–Eur. J.*, 2013, **19**, 14279–14285.
52 C. G. Silva, A. Corma and H. García, *J. Mater. Chem.*, 2010, **20**, 3141–3156.
53 Y. Kamakura, S. Yasuda, N. Hosokawa, S. Nishioka, S. Hongo, T. Yokoi, D. Tanaka and K. Maeda, *ACS Catal.*, 2022, **12**, 10172–10178.
54 A. M. P. Peedikakkal, Y.-M. Song, R.-G. Xiong, S. Gao and J. J. Vittal, *Eur. J. Inorg. Chem.*, 2010, 3856–3865.
55 K. Biradha, M. Sarkar and L. Rajput, *Chem. Commun.*, 2006, 4169–4179.
56 O.-S. Jung, S. H. Park, K. M. Kim and H. G. Jang, *Inorg. Chem.*, 1998, **37**, 5781–5785.
57 A. N. Khlobystov, A. J. Blake, N. R. Champness, D. A. Lemenovskii, A. G. Majouga, N. V. Zyk and M. Schröder, *Coord. Chem. Rev.*, 2001, **222**, 155–192.
58 J. H. Kim, J. M. Bae, H. G. Lee, N. J. Kim, K.-D. Jung, C. Kim, S.-J. Kim and Y. Kim, *Inorg. Chem. Commun.*, 2012, **22**, 1–5.
59 N. Dannenbauer, P. R. Matthes, T. P. Scheller, J. r. Nitsch, S. H. Zottnick, M. S. Gernert, A. Steffen, C. Lambert and K. Müller-Buschbaum, *Inorg. Chem.*, 2016, **55**, 7396–7406.
60 A. N. Pârvulescu, G. Marin, K. Suwinska, V. C. Kravtsov, M. Andruh, V. Pârvulescu and V. I. Pârvulescu, *J. Mater. Chem.*, 2005, **15**, 4234–4240.
61 X.-K. Wang, J. Liu, L. Zhang, L.-Z. Dong, S.-L. Li, Y.-H. Kan, D.-S. Li and Y.-Q. Lan, *ACS Catal.*, 2019, **9**, 1726–1732.
62 R. Kusama, S. Kajimoto, I. Rzeznicka and H. Fukumura, Structures and emission properties of gold-1,2-di-(4-pyridyl)-ethylene complexes, 2015, 3P050, **http://molsci.center.ims.ac.jp/area/2015/PDF/pdf/3P050_w.pdf**.
63 C. Xu, W. Chen, J. Wang, Q. Wu, P. Wu and L. Tang, *J. Inorg. Organomet. Polym. Mater.*, 2023, **33**, 885–894.

Open Access Article. Published on 30 2025. Downloaded on 29.11.2025 13:58:24.
This article is licensed under a Creative Commons Attribution-NonCommercial 3.0 Unported Licence.

64 C.-c. Wang, H.-p. Jing and P. Wang, *J. Mol. Struct.*, 2014, **1074**, 92–99.
65 J. Zhang, C.-C. Wang, P. Wang, X.-X. Guo and S.-J. Gao, *Transition Met. Chem.*, 2016, **41**, 637–645.
66 J. Suebphanpho, S. Wannapaiboon, S. Youngme and J. Boonmak, *Cryst. Growth Des.*, 2020, **20**, 7439–7449.
67 F. Zheng, L. Guo, B. Gao, L. Li, Z. Zhang, Q. Yang, Y. Yang, B. Su, Q. Ren and Z. Bao, *ACS Appl. Mater. Interfaces*, 2019, **11**, 28197–28204.
68 Rigaku, *CrystalClear-SM Expert 2.0 r7*, 2011.
69 Rigaku, *CrysAlisPro 1.171.41.113a*, 2021.
70 Rigaku, *Rigaku Journal*, 2016, **32**, 31–34.
71 G. M. Sheldrick, *Acta Crystallogr., Sect. A*, 1990, **46**, 467–473.
72 Bruker, *SAINT*, Bruker AXS Inc., Madison, Wisconsin, USA, 1999.
73 L. J. Bourhis, O. V. Dolomanov, R. J. Gildea, J. A. Howard and H. Puschmann, *Acta Crystallogr., Sect. A:Found. Adv.*, 2015, **71**, 59–75.
74 O. V. Dolomanov, L. J. Bourhis, R. J. Gildea, J. A. Howard and H. Puschmann, *J. Appl. Crystallogr.*, 2009, **42**, 339–341.
75 G. M. Sheldrick, *Acta Crystallogr., Sect. C:Struct. Chem.*, 2015, **71**, 3–8.
76 S. Yoshioka, Y. Inokuma, M. Hoshino, T. Sato and M. Fujita, *Chem. Sci.*, 2015, **6**, 3765–3768.
77 C. F. Macrae, I. J. Bruno, J. A. Chisholm, P. R. Edgington, P. McCabe, E. Pidcock, L. Rodriguez-Monge, R. Taylor, J. Streek and P. A. Wood, *J. Appl. Crystallogr.*, 2008, **41**, 466–470.
78 M. A. Withersby, A. J. Blake, N. R. Champness, P. A. Cooke, P. Hubberstey, A. L. Realf, S. J. Teat and M. Schröder, *J. Chem. Soc., Dalton Trans.*, 2000, 3261–3268.
79 M. Mikuriya, R. Indrawati, R. Hashido, S. Matsubara, C. Nakamura, D. Yoshioka, K. Yokota, M. Fukuzaki and M. Handa, *Magnetochemistry*, 2018, **4**, 22.
80 C.-C. Wang, F.-C. Liu, C.-K. Chiu, Y. Song, S.-C. Wang, Y. Wang, G.-H. Lee, H.-S. Sheu and E.-C. Yang, *CrystEngComm*, 2011, **13**, 118–123.
81 J. Van Niekerk and F. Schoening, *Acta Crystallogr.*, 1953, **6**, 227–232.
82 G. M. Brown and R. Chidambaram, *Acta Crystallogr. Sect. B Struct. Crystallogr. Cryst. Chem.*, 1973, **29**, 2393–2403.
83 M. A. Spackman and D. Jayatilaka, *CrystEngComm*, 2009, **11**, 19–32.
84 A. F. Shaidullina, A. R. Sharipova, M. Y. Volkov, L. I. Savostina, L. G. Gafiyatullin, O. A. Turanova and A. N. Turanov, *Photochem. Photobiol.*, 2023, **99**, 1378–1383.
85 P. Makuła, M. Pacia and W. Macyk, *J. Phys. Chem. Lett.*, 2018, **9**(23), 6814–6817.
86 J. Bardeen, W. Brattain and W. Shockley, *J. Chem. Phys.*, 1946, **14**, 714–721.
87 K. Gelderman, L. Lee and S. Donne, *J. Chem. Educ.*, 2007, **84**, 685.
88 A. J. Botz, M. Nebel, R. A. Rincón, E. Ventosa and W. Schuhmann, *Electrochim. Acta*, 2015, **179**, 38–44.
89 M. Lu, *Supercapacitors: Materials, Systems, and Applications*, John Wiley & Sons, 2013.
90 J. He, J. Wang, Y. Chen, J. Zhang, D. Duan, Y. Wang and Z. Yan, *Chem. Commun.*, 2014, **50**, 7063–7066.
91 J. M. Thornton and D. Raftery, *New and Future Developments in Catalysis: Chapter 8. Photocatalysts for Solar Hydrogen Conversion*, Elsevier Inc. Chapters, 2013.
92 K. Fabrizio, K. N. Le, A. B. Andreeva, C. H. Hendon and C. K. Brozek, *ACS Mater. Lett.*, 2022, **4**, 457–463.
93 C. Bock, J. Connor, A. Gutierrez, T. J. Meyer, D. Whitten, B. Sullivan and J. Nagle, *J. Am. Chem. Soc.*, 1979, **101**, 4815–4824.
94 T.-A. Quach, V. N. Gopalakrishnan, J. Becerra, D.-T. Nguyen, J. M. Ahad, S. Mohan and T.-O. Do, *Catal. Today*, 2023, **421**, 114218.
95 S.-L. Xie, J. Liu, L.-Z. Dong, S.-L. Li, Y.-Q. Lan and Z.-M. Su, *Chem. Sci.*, 2019, **10**, 185–190.
96 J. E. Pander III, A. Fogg and A. B. Bocarsly, *ChemCatChem*, 2016, **8**, 3536–3545.
97 A. Call, M. Cibian, K. Yamauchi and K. Sakai, *Sustainable Energy Fuels*, 2022, **6**, 2160–2164.
98 B. Kurpil, Y. Markushyna and A. Savateev, *ACS Catal.*, 2019, **9**, 1531–1538.
99 L. Mintrop, J. Windisch, C. Gotzmann, R. Alberto, B. Probst and P. Kurz, *J. Phys. Chem. B*, 2015, **119**, 13698–13706.
100 C. E. Housecroft, and A. G. Sharpe, *Inorganic Chemistry*, Pearson, Harlow, 4th edn, 2012, pp. 639–777.
101 A. Call, M. Cibian, K. Yamamoto, T. Nakazono, K. Yamauchi and K. Sakai, *ACS Catal.*, 2019, **9**, 4867–4874.

 This journal is © The Royal Society of Chemistry 2025